

---

# A Magnetorheological-Polishing-Based Approach for Studying Precision Microground Surfaces of Tungsten Carbides

## Introduction

Tungsten carbide (WC) hard metals exhibit a unique combination of hardness and toughness, which makes them desirable engineering materials for wear-resistance applications such as cutting and milling tools.<sup>1</sup> The mixing of the hard and brittle WC particles with the more soft and ductile binder produces a composite with optimal mechanical properties.<sup>2,3</sup>

The metallic binder of cemented carbides is usually cobalt; however, when the application exposes the material to an acid environment, a nickel-based binder is favored for its better corrosion resistance. Another approach for improving corrosion resistance is to reduce the amount of binder,<sup>4</sup> namely binderless carbides. This work focuses on Ni-bonded and binderless cemented carbides. All of these materials are nonmagnetic.

The use of tungsten carbide materials in optical systems<sup>5</sup> as either mold masters<sup>6</sup> or mirrors<sup>7</sup> is the motivation behind achieving nanoscale surface roughness from grinding and subsequently polishing. Surface roughness is closely related to the wear mechanism of the material. SEM images of the ground surfaces exposed the similarities between the wear behavior of Ni-bonded and Co-bonded materials, in particular, the formation of a deformed surface layer because of the extrusion of the nickel binder between the WC grains, as described for Co-bonded<sup>3,8</sup> materials. Previous studies by others show that although the tungsten carbide wear mechanism involves brittle fracture, fatigue, and plastic deformation, it is dominated by the extrusion of the soft binder between WC grains.<sup>1,8-10</sup> Redeposited binder and WC debris cover the ground surface, forming a deformed layer<sup>11</sup> that is also known as subsurface damage, which masks the true surface roughness induced by grinding. In a recent study, the deformed layer depth was reported to be near 1.5  $\mu\text{m}$  for ground WC-10 wt% Co composites (20- $\mu\text{m}$  grains) with a 91- $\mu\text{m}$  (approximately 34- $\mu\text{m}$  nominal abrasive size) diamond wheel.<sup>11</sup> Because of the inhomogeneity of the composite carbide grains and the diamond distribution on the grinding wheel, however, the amount of damaged material that needed to be removed during the subsequent polishing stage could not be determined. Therefore, a more determinis-

tic technique is needed to measure the deformed layer depth after grinding.

The goal of this work is a better understanding of the correlation between the response of tungsten carbide hard metals to microgrinding and nanopolishing with the resulting surface microroughness. In recent work done by Randi *et al.*,<sup>12</sup> it was demonstrated that magnetorheological finishing (MRF) can be used to determine subsurface damage depth for optical crystals and glasses. Because both Ni-bonded and the binderless cemented carbides are nonmagnetic, they are excellent candidates for MRF. In this study, we demonstrate that MRF spots can be placed on ground nonmagnetic tungsten carbides and that the spots can be used to evaluate the depth of the damaged layer. We focus on five nonmagnetic WC materials, which include four WC-Ni composites with variations in nickel binder content and one binderless sample, all with different grain sizes.

## Experimental Procedures

### 1. Tungsten Carbide

Five commercial nonmagnetic WC samples were used for this study. The materials are commercially designated as BC12N,<sup>13</sup> K801,<sup>14</sup> M45,<sup>15</sup> M10,<sup>15</sup> and Cerbide.<sup>16</sup> They were selected on the basis of their nickel content and grain size as well as their mechanical properties. The WC grain sizes varied from 0.2  $\mu\text{m}$  to 7  $\mu\text{m}$ , and the nickel binder concentration varied from none (in the binderless carbide) to 12.5 wt%. Hardness measurements were obtained on all materials using a Tukon micro-indenter equipped with a Vickers diamond indenter and a microscope (50 $\times$  objective), averaging the diagonals of five random indents on the surface with a load of 1 kg and a duration of 15 s. The applied load was enough to produce radial cracks<sup>17</sup> at the corners of the indentations in M10 and Cerbide. These two materials have a low ductility index (DI)<sup>18</sup> ( $K_c/H_v$ )<sup>2</sup>, where  $K_c$  is the fracture toughness ( $\text{kg}/\text{mm}^2 \text{m}^{0.5}$ ) and  $H_v$  is the Vickers hardness ( $\text{kg}/\text{mm}^2$ ). Fracture-toughness values were calculated from the observed cracks using the Evans correlation.<sup>19</sup> The Laugier correlation<sup>20</sup> for WC material ( $H_v \geq 10,000$  MPa) was applied to calculate the fracture toughness

for the other three materials, which did not exhibit cracking under 1-kg loads. Relevant microstructural, mechanical, and physical properties are listed in Table 105.IV, ranked according to decreasing value of the ductility index.

2. Grinding Experiments

The grinding experiments were performed on the OptiPro SX50 platform,<sup>21</sup> a deterministic computer numerical control (CNC) ultraprecision grinding machine. The SX50 is capable of generating rotationally symmetric spherical and flat surfaces. For all our grinding experiments, a contour-tool grinding configuration for flat surfaces was used (Fig. 105.55) with three different diamond tools, rough, medium, and fine (40- $\mu\text{m}$ , 10- to 20- $\mu\text{m}$ , 2- to 4- $\mu\text{m}$  grit size, respectively). Both the rough and medium tools were made of a bronze matrix while the fine tool matrix was resin. To avoid taking the part off the machine between operations, the tools were trued and dressed in advance using  $\text{Al}_2\text{O}_3$  dressing sticks that were 320 or 800 grit (29- to 32- $\mu\text{m}$  and 9- to 12- $\mu\text{m}$  grit size, respectively). Table 105.V lists the grinding conditions used where  $\Omega_t$  is the wheel speed, and  $\Omega_w$  is the spindle speed.

Each workpiece was glued on a steel base with hot wax and then placed in the grinding machine parallel to the tool axis of rotation. Water-oil emulsion coolant (Opticut solution 5%, 9–10 pH)<sup>22</sup> was delivered to the interface between the workpiece and tool to avoid burn out and thermal damage. The grinding was done with two passes for each tool; i.e., the total material removed depth of cut per tool was 200, 40, and 10  $\mu\text{m}$  (rough, medium, and fine tools, respectively). For example, the

fine grinding was done only after the part had gone through two-pass cycles with the rough and mediums tools. Finally, the workpieces were cleaned using acetone.

3. Investigation of the Deformed Layer

a. Etching of ground surface. After the materials were ground, a small area on the processed surface was etched to remove the deformed nickel binder. The etching solution contained 15-ml deionized water, 15-ml glacial acetic acid, 60-ml hydrochloric acid/32%, and 15-ml nitric acid/65%.<sup>11</sup> Each surface was etched for 3 min, then rinsed with water, and finally cleaned with acetone.

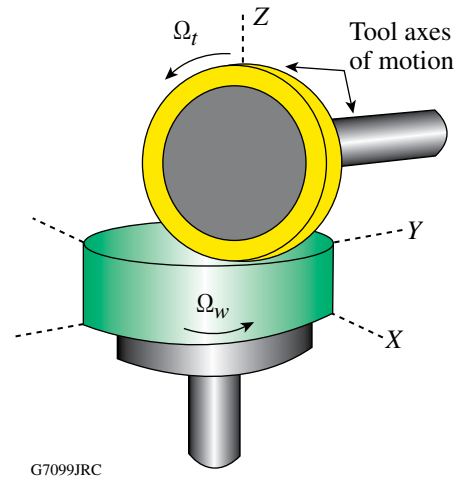


Figure 105.55 Schematics of the contour-grinding configuration adapted from Ref. 30.

Table 105.IV: Material microstructural and mechanical properties.<sup>(a)</sup>

Material ID	Dimensions (mm) per number of samples	Grain size ( $\mu\text{m}$ )	Ni wt%	Hardness Rockwell A	Young's modulus $E$ (GPa) <sup>(c)</sup>	Vickers hardness $H_v$ (GPa) <sup>(e)</sup>	Fracture toughness $K_c$ ( $\text{MPa} \sqrt{m}$ )	Ductility index DI $(K_c/H_v)^2$ ( $\mu\text{m}$ )
BC12N <sup>13</sup>	30 × 26/2	1.0	12	87.5–89.0	(614) <sup>(d)</sup>	12.01±0.13	12.98 <sup>(g)</sup>	1.17
K801 <sup>14</sup>	40 $\Phi$ /3	7.0	6.3	90.7	618	13.71±0.17	10.15 <sup>(g)</sup>	0.55
M45 <sup>15</sup>	30.01 $\Phi$ /3	0.6–1.3	12.5 <sup>(b)</sup>	89.5	500	14.78±0.17	8.06 <sup>(g)</sup>	0.30
M10 <sup>15</sup>	30.01 $\Phi$ /3	0.2–0.6	9.5 <sup>(b)</sup>	92.5	510	18.54±0.2	6.35±0.10 <sup>(e),(f)</sup>	0.12
Cerbide <sup>16</sup>	56 × 32/2	0.4	None	95.5	620	24.72±0.61	5.75±0.04 <sup>(e),(f)</sup>	0.05

<sup>(a)</sup>Catalog values, unless specified otherwise. <sup>(b)</sup>Approximate values from EDS measurements. <sup>(c)</sup>Converted from PSI. <sup>(d)</sup>Estimated value. <sup>(e)</sup>Average of five Vickers indentations at 1 kgf. <sup>(f)</sup>Evans.<sup>19</sup> <sup>(g)</sup>Calculated values by using Laugier's<sup>20,32,33</sup> correlation  $K_c = 2.15 \times 10^6 (E/H_v)^{0.6} (1 + 0.012 E/H_v)^{0.6} H_v^{-1.5}$  for WC-Co composites containing a ductile (i.e., binder) phase, where  $E$  is the Young's modulus in units of MPa and  $H_v$  is the Vickers hardness in units of MPa for  $H_v \geq 10,000$  MPa.

Table 105.V: Contour grinding conditions used on the OptiPro SX50 in a single pass.<sup>(a)</sup>

Tool grit size ( $\mu\text{m}$ )	Depth of cut ( $\mu\text{m}$ )	In-feed (Z-axis) (mm/min)	Duration of single pass (s)	Cross feed (X-axis) (mm/min)	Duration of single pass (min)
40 <sup>(b)</sup>	100	0.5	12	1.0	30–40
10–20 <sup>(b)</sup>	20	0.5	2.4	1.0	30–40
2–4 <sup>(c)</sup>	5	0.5	0.6	5.0	6–8

<sup>(a)</sup>The following parameters remained constant: wheel speed,  $\Omega_t = 6800$  rpm and work spindle speed,  $\Omega_w = 100$  rpm.

<sup>(b)</sup>Bronze-bonded, 75 diamond concentration. <sup>(c)</sup>Resin-bonded, 75 diamond concentration.

**b. Processed surface spotting.** Magnetorheological finishing (MRF)<sup>23,24</sup> is a commercial polishing process for the manufacturing of precision optics. It was used in our experiment to measure the depth of the deformed layer from grinding and the quality of the subsurface subsequently exposed. Specifically, we used a MRF research platform called the spot-taking machine,<sup>25</sup> which polishes spots onto the surface of a nonrotating part by lowering the part surface into contact with a rotating magnetic fluid ribbon under CNC control. The material removal rate is determined from the amount of material removed, i.e., ratio of spot volume, divided by the spotting time. The MRF fluid used in this work consisted of an aqueous mixture of nonmagnetic nanodiamond<sup>26</sup> abrasives, magnetic carbonyl iron, water, and stabilizers. Machine parameters such as the magnetic field strength ( $\sim 2\text{--}3$  kG), wheel speed (250 rpm), pump speed (125 rpm), ribbon height (1.6 mm), and depth of the part penetrating into the ribbon (0.3 mm) were kept constant and the spotting time was varied. Spotting was done on unetched regions of rough-ground, medium-ground, and fine-ground surfaces of each material. Multiple spots with time durations of 3, 6, 12, 18, and 40 min were taken on subsets of the generated surfaces as described in **Subsurface Damage Evaluation from the Spotting Experiment** (p. 56).

#### 4. Microscopy of Processed Surfaces

Surfaces were studied using a white-light interferometer, scanning electron microscope (SEM), contact profilometer, and atomic force microscope (AFM). Before analyzing the surfaces, the samples were ultrasonically cleaned in acetone and then rinsed with alcohol; surfaces were dried using a nitrogen gun after ultrasonication and after rinsing.

Metrology was conducted as follows:

- Average microroughness data [peak-to-valley (p–v), and root mean square (rms)] were obtained with a Zygo NewView 5000 noncontacting white-light interferometer<sup>27</sup> over

five  $350\text{-}\mu\text{m}$  by  $250\text{-}\mu\text{m}$  areas randomly distributed across ground and unetched areas. This instrument has a lateral resolution of  $\sim 1\ \mu\text{m}$  and a vertical resolution of  $\sim 0.3$  nm. Data were similarly obtained inside MRF spots; see details in **Subsurface Damage Evaluation from the Spotting Experiment** (p. 56).

- The morphologies of the processed surfaces after grinding, etching, and MRF were analyzed using a LEO 982 FE SEM equipped with a secondary electron detector, a backscatter detector, and also an energy dispersive x-ray spectroscopy detector (EDS). The preferred imaging configuration was a mix signal of the in-lens and in-chamber secondary electron detectors. The EDS x-ray detector was used to approximate Ni content for WC samples M10 and M45.
- The Taylor Hobson TalySurf 2 PGI stylus profilometer<sup>28</sup> was used to perform 3-D scans of the MRF spots, which were then used to extract the spot physical dimensions, i.e., spot volume, peak removal depth, and spot profile. The stylus tip is a cone with a  $60^\circ$  angle and a  $2\text{-}\mu\text{m}$  spherical tip radius of curvature. The instrument has a 12-nm vertical resolution.
- Additional surface scans for selected spots were taken on the Digital Instruments/Veeco Metrology Dimension 3100S-1 AFM<sup>29</sup> over three  $10\text{-}\times\text{ }10\text{-}\mu\text{m}^2$  areas randomly distributed across areas in spots where the deepest point of fluid penetration (ddp) occurred, as discussed below. This instrument has a vertical noise resolution of less than  $0.5\ \text{\AA}$ .

### Experimental Results

#### 1. Surface Roughness and Surface Morphology from Grinding

Surface-roughness data for all materials after each grinding stage were taken using the white-light interferometer. Results are reported in Table 105.VI for all surfaces in their as-ground state.

The data given in Table 105.VI show the expected result of smoothing with decreasing diamond abrasive size. The p-v surface roughness varied from ~3280 nm (BC12N) to ~5820 nm (M10) with the coarse tool, from ~550 nm (K801) to ~3850 nm (M10) with the medium tool, and from ~53 nm (M45) to ~86 nm (BC12N) with the fine tool. The smoothest surface after fine grinding was ~7-nm rms (M45).

After the samples were ground with the fine resin tool (2- to 4-μm grit size), a “mirror quality” surface finish was achieved, as shown in Fig. 105.56. Surface roughness measurements were below 100 nm p-v and below 13-nm rms for all materials, as seen in Fig. 105.57. All surfaces had some degree of midspatial frequency artifacts (i.e., cutter marks), however, with a better surface for the circular-shaped parts over the rectangular ones because of the interrupted cut during part rotation. All the grinding tools showed some degree of material accretion from the workpiece.

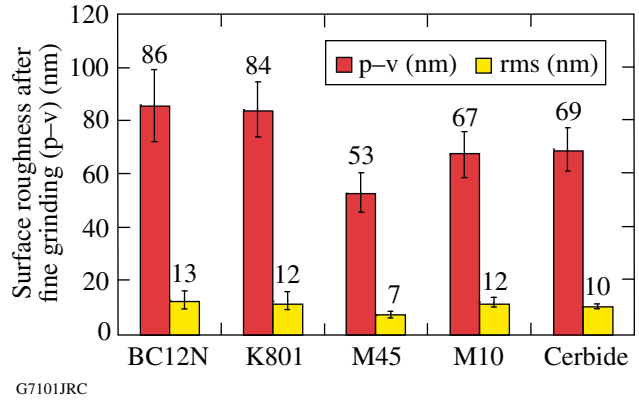


Figure 105.57 Surface roughness of fine-ground surfaces (2- to 4-μm grit size) versus WC material type. The error bars represent the standard deviation of five areal measurements.

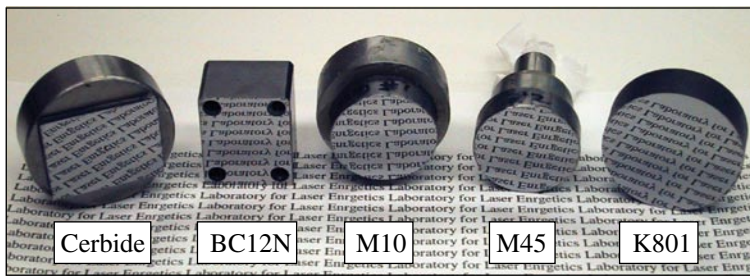


Figure 105.56 Optical image of the “mirror-like” fine-ground WC material after fine grinding (2- to 4-μm grit size). Surface-roughness measurements were below 100-nm p-v and below 13-nm rms.

Table 105.VI: Tungsten carbide surface roughness under contour grinding conditions using rough, medium, and fine tools. Measurements were taken on the white-light interferometer.

	BC12N	K801	M45	M10	Cerbide
Rough tool (40-μm grit size)					
p-v (nm)	3280±194	3802±289	3915±371	5823±975	3857±326
rms (nm)	154±19	151±30	286±113	695±289	242±67
Medium tool (10- to 20-μm grit size)					
p-v (nm)	2372±59	552±136	1915±175	3854±265	3322±153
rms (nm)	72±4	27±4	65±11	195±14	142±9
Fine tool (2- to 4-μm grit size)					
p-v (nm)	86±13	84±10	53±7	67±9	69±8
rms (nm)	13±3	12±3	7±1	12±2	10±1

SEM images illustrated that the topography of the ground surfaces, from rough to fine, were in agreement with the surface-roughness measurements. Figure 105.58 gives the typical morphology of rough-ground surfaces (rough tool, 40- $\mu\text{m}$  grit size). Fragmented WC particles and plastically deformed material (arrows 1 and 2) are observed on the ground surfaces, forming a deformed surface layer, as described by Hegeman *et al.*<sup>11</sup> Material K801, with an average grain size of 7  $\mu\text{m}$  (the coarsest of all materials studied, see Table 105.IV), showed some pullout of individual grains. Figure 105.58(a) shows that the deformed layer is absent in regions of grain pullout<sup>11</sup> (arrow 3). We observed different morphologies of the deformed layer for the different materials. The deformed layer appears smoother for materials with a submicron grain size (0.2 to 0.6  $\mu\text{m}$ ) [Fig. 105.58(c) and 105.58(d)]. The plastic deformation of the binderless material is similar to that for the Ni-bonded materials, i.e., fragmented and plastically deformed WC grains (arrows 1 and 2, respectively), suggesting that only small amounts of the binder are present in the deformed surfaces, compared to the bulk material, as observed by Yin *et al.*<sup>5</sup> and Hegeman *et al.*<sup>11</sup> Therefore, the deformed surfaces mostly consist of plastically deformed WC grains.

Figure 105.59 shows SEM images of the fine-ground surfaces that reveal the material microstructure, i.e., the carbide grains and the nickel binder. Fragmented traces of the WC grains are visible inside “pockets” between grains (arrow 1). Traces from single diamond scratches and tool marks<sup>30</sup> can be seen at arrow 2.

All ground surfaces were etched in small regions to remove the nickel binder, exposing the subsurface of the deformed layer. In some areas on the surface the plastically deformed material, as well as WC debris, was removed, leaving small etching pits. The etching procedure also removed bronze and resin tool residue from the surface. Figure 105.60 shows a SEM image of a typical etching pit in a fine-ground surface, which exposed the subsurface of the ground surface. It can be clearly observed that almost all the nickel binder between grains was removed along with fragmented WC particles that were embedded. High-magnification images of the etched pits [Fig. 105.61(a)] showed subsurface damage in the form of cracked grains after rough grinding (40  $\mu\text{m}$ ). Figures 105.61(b) and 105.61(c), for both medium and fine tools (10- to 20- $\mu\text{m}$ , and 2- to 4- $\mu\text{m}$  grit size, respectively), reveal no evidence of

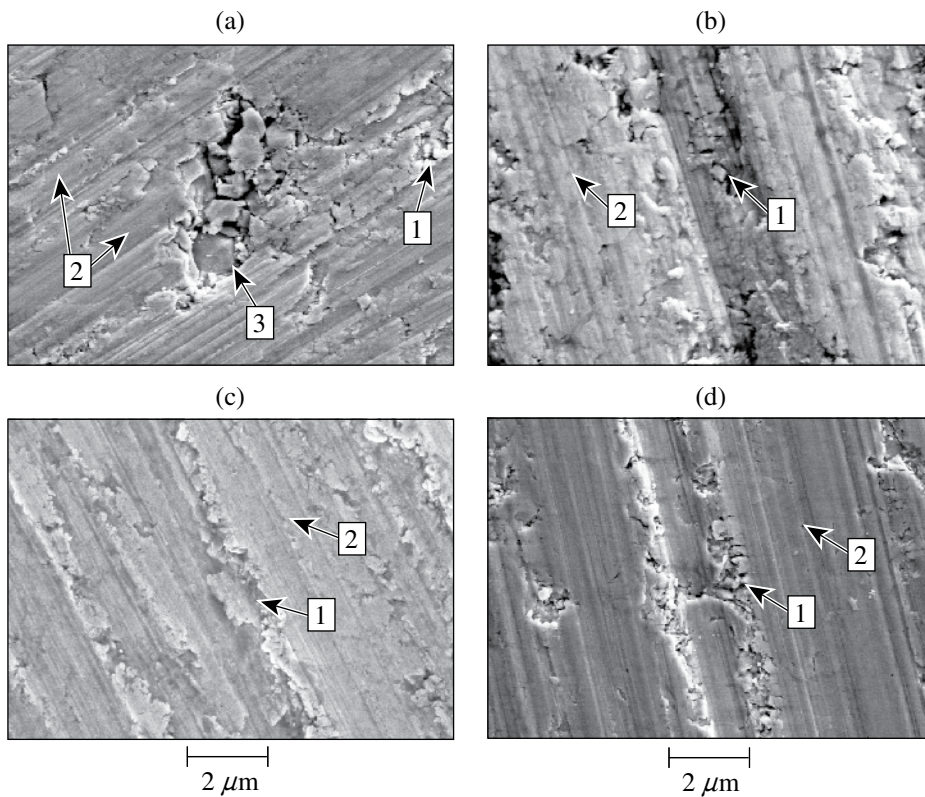


Figure 105.58  
SEM images of typical rough-ground surfaces (40- $\mu\text{m}$  grit size). Average grain sizes are (see Table 105.IV) (a) K801, 6.3 wt% Ni, 7  $\mu\text{m}$ ; (b) M45, 12.5 wt% Ni, 0.6–1.3  $\mu\text{m}$ ; (c) M10, 9.5 wt% Ni, 0.2–0.6  $\mu\text{m}$ ; and (d) Cerbide, 0.4  $\mu\text{m}$ . Arrows represent (1) fragmented WC, (2) plastically deformed WC, and (3) the pullout of an individual grain.

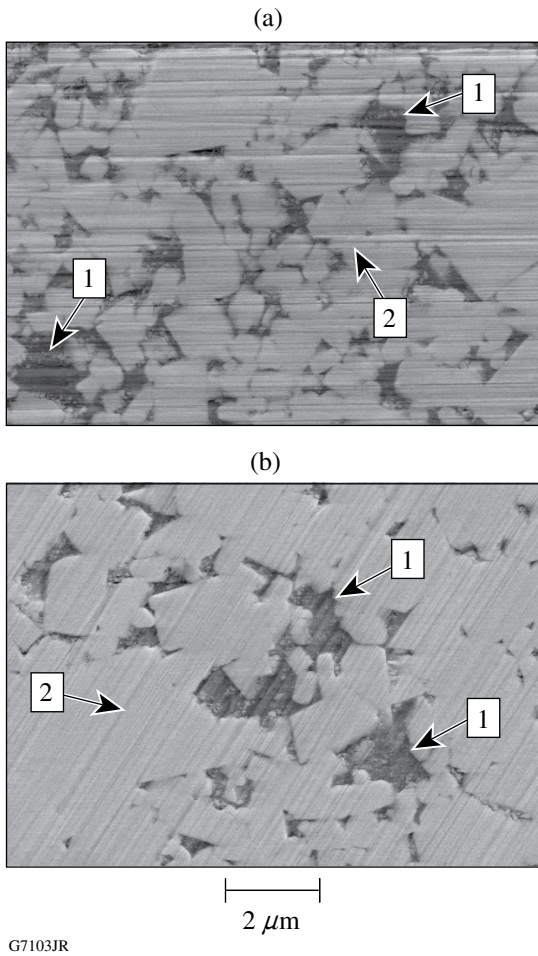


Figure 105.59  
SEM images of fine-ground WC surfaces (2- to 4- $\mu\text{m}$  grit size). (a) BC12N, 12 wt% Ni, 1- $\mu\text{m}$  grain size and (b) K801, 6 wt% Ni, 7- $\mu\text{m}$  grain size (see Table 105.IV). Arrows represent (1) "pockets" between grains and (2) single diamond scratches/tool marks.

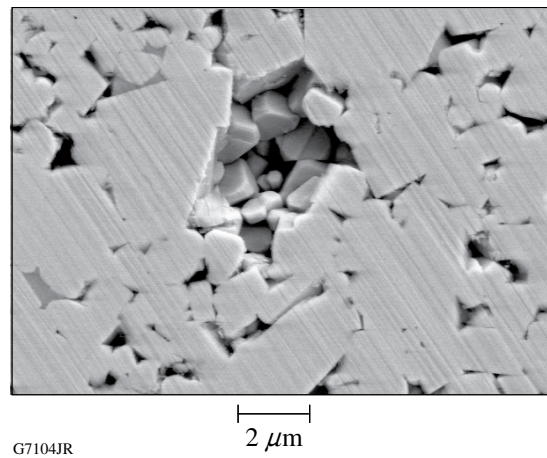


Figure 105.60  
SEM images of a typical etched pit in a fine-ground (2- to 4- $\mu\text{m}$  grit size) WC surface, K801, 6 wt% Ni, 7- $\mu\text{m}$  grain size (see Table 105.IV).

fractured WC grains, suggesting that the wear mechanism is controlled by plastic flow. The Carbide ground surface was not affected by the etching, as expected.

## 2. Subsurface Damage Evaluation from the Spotting Experiment

MRF spots of various durations were taken on all rough-ground surfaces and 6-min spots were taken on both fine- and medium-ground surfaces. Figure 105.62 shows a typical 3-D map of a polished MRF spot indicating the spot leading edge (MRF fluid ribbon entrance/penetration point into the material), spot ddp (deepest point of MRF fluid penetration), and spot trailing edge (point of the fluid leaving the part) using the profilometer. From analyzing the 3-D scans, we were able to extract spot profiles, which were then used to identify the

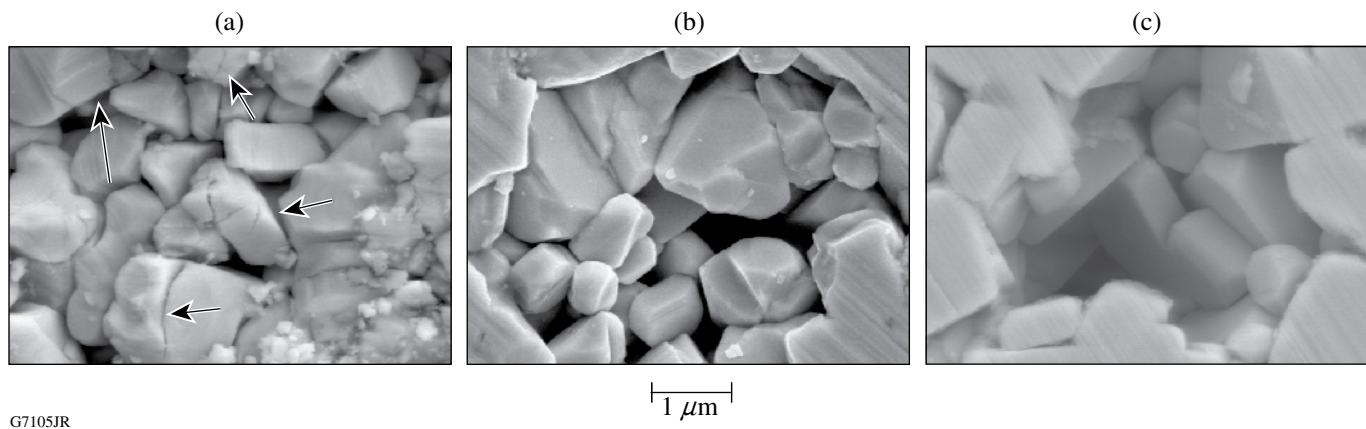
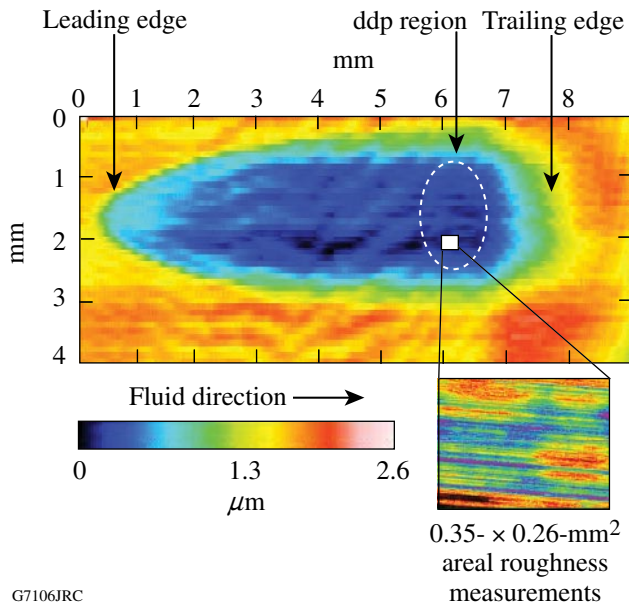


Figure 105.61  
High-magnification SEM images of etching pits in ground WC composites showing the (a) rough, (b) medium, and (c) fine ground. The arrows in (a) point at cracks in the carbide phase. The materials are (see Table 105.IV) (a) BC12N, 12 wt% Ni, 1- $\mu\text{m}$  grain size and (b) and (c) K801, 6 wt% Ni, 7- $\mu\text{m}$  grain size.



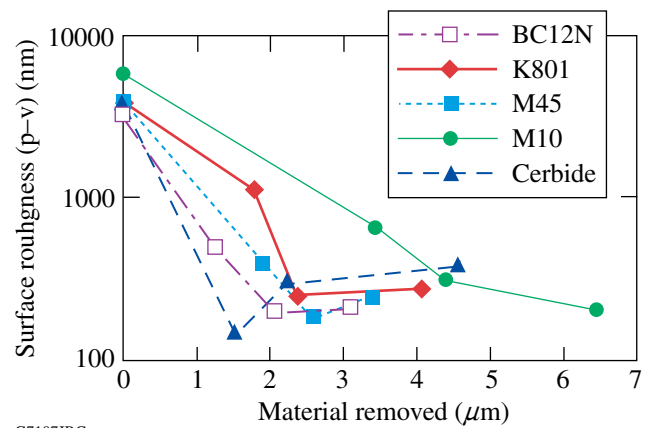
G7106JRC

Figure 105.62

3-D image of an MRF spot taken with a Taylor Hobson TalySurf profilometer on WC M10 for 6 min. Arrows indicate the spot leading edge (MRF fluid ribbon entrance/penetration point into the material), spot dcp (deepest point of MRF fluid penetration), spot trailing edge (where the MRF fluid leaves the material), and fluid flow direction. The white rectangle within the dcp region represents one of the five sites over which surface roughness was measured using white-light interferometry.

dcp. The spot volume and maximum depth dcp are listed in Table 105.VII. These spot profiles were not similar to profiles typically observed for other optical glasses and crystals.<sup>25</sup>

After the location of the spot dcp was identified, surface-roughness measurements at five random locations within the dcp region were taken with the white-light interferometer. Results are given in Table 105.VII. To investigate the amount of material needed to be removed by the MRF spot (i.e., the depth of the deformed layer from the grinding cycles), we plotted the evolution of the surface roughness with the maximum amount of material removed (see Fig. 105.63). It was observed that the initial surface roughness is removed for BC12N, K801, M45, and Cerbide when the MRF penetrates past 2.1 to 2.6  $\mu\text{m}$  of the deformed layer thickness. However, surface roughness eventually increased with increasing MRF material removal. A monotonic decrease in surface roughness with increasing material removal was noted for M10. SEM images taken within the dcp region of the optimal spot (i.e., least roughness) confirmed that the deformed layer induced by grinding is completely removed by the MRF process (see Fig. 105.64). It should be emphasized that the clean surfaces shown in Fig. 105.64 are due entirely to the MRF process, without any pre- or post-etching.



G7107JRC

Figure 105.63

Evaluation of surface roughness, p-v (nm) semilog, versus MRF spot material removed ( $\mu\text{m}$ ). The starting condition is the rough-ground surface (p-v roughness in the range of 3.3 to 5.8  $\mu\text{m}$ ). After removing 2 to 3  $\mu\text{m}$  of material from the surface, the p-v roughness decreases to 180–310 nm.

Table 105.VII also demonstrates the influence of the initial surface roughness on the surface response inside MRF spots. For initial rough-ground surfaces, surface roughness improved after MRF penetrated 2.1 to 2.6  $\mu\text{m}$  past the deformed layer for BC12N, K801, M45, and Cerbide and 4.4  $\mu\text{m}$  for M10. The p-v surface roughness varied from ~185 nm (M45) to ~303 nm (Cerbide). For initial fine-ground surfaces, the p-v surface roughness varied from ~29 nm (Cerbide) to ~86 nm (BC12N). The smoothest surface for the initial fine-grinding surface conditions was ~3.4-nm rms (Cerbide). We also observed an increase in surface roughness inside MRF spots for materials with a higher ductility index, however, after 1 to 1.8  $\mu\text{m}$  was removed (by the MRF spot).

### 3. MRF Surface Evolution with Increasing Depth Removed

Further study of the surface after MRF polishing was done for rough-ground K801 with an ~3802-nm initial p-v surface roughness [see Fig. 105.65(a)] where additional MRF spots at varying depths of MRF removal were taken. Figure 105.65 shows that after 1.8  $\mu\text{m}$  of material is removed by the MRF spot, the deformed layer induced is not completely removed [see Fig. 105.65(b)], in agreement with the surface-roughness values. With a longer MRF spotting time, a total of 2.4- $\mu\text{m}$  of material was removed [see Fig. 105.65(c)], an amount sufficient to expose the undisturbed subsurface. However, additional material removal slightly increases the surface roughness. Similar behavior is observed by monitoring the evolution of the rms surface roughness.

Table 105.VII: Summary results of the spotting experiments. Surface-roughness measurements were taken at five random locations within a spot ddp with the white-light interferometer. The maximum spot depth and volume removed were extracted from the profilometer 3-D scans.

Spot time (min)		BC12N	K801	M45	M10	Cerbide
Initial surface conditions: rough ground						
3	p-v (nm)	505±37	1106±143	399±52	657±216	146±17
	rms (nm)	43±5	46±5	47±5	83±16	25±5
	Depth (μm)	1.3±0.08	1.8±0.01	1.9±0.08	3.4±0.28	1.5±0.03
	Vol. (mm <sup>3</sup> )	0.01±0.0	0.01±0.0	0.01±0.0	0.02±0.01	0.01±0.0
6	p-v (nm)	204±10	248±24	185±26	312±20	303±20
	rms (nm)	35±2	39±5	31±11	61±6	55±11
	Depth (μm)	2.1±0.01	2.4±0.03	2.6±0.05	4.4±0.21	2.3±0.12
	Vol. (mm <sup>3</sup> )	0.02±0.0	0.02±0.0	0.02±0.0	0.03±0.01	0.03±0.0
12	p-v (nm)	—	287±31	—	—	—
	rms (nm)	—	43±10	—	—	—
	Depth (μm)	—	3.2±0.07	—	—	—
	Vol. (mm <sup>3</sup> )	—	0.03±0.0	—	—	—
18	p-v (nm)	212±51	276±60	240±32	205±50	383±56
	rms (nm)	33±5	45±12	40±11	39±10	63±14
	Depth (μm)	3.1±0.08	4.0±0.09	3.4±0.31	6.4±0.06	4.6±0.13
	Vol. (mm <sup>3</sup> )	0.02±0.0	0.04±0.0	0.03±0.0	0.06±0.01	0.04±0.0
40	p-v (nm)	—	395±134	—	—	—
	rms (nm)	—	53±9	—	—	—
	Depth (μm)	—	8±0.13	—	—	—
	Vol. (mm <sup>3</sup> )	—	0.08±0.0	—	—	—
Initial surface conditions: medium ground						
6	p-v (nm)	215±5	456±33	107±13	113±21	114±20
	rms (nm)	35±2	27±5	16±1	19±2	20±3
	Depth (μm)	1.8±0.05	1.5±0.03	1±0.04	1.9±0.10	1.5±0.06
	Vol. (mm <sup>3</sup> )	0.02±0.0	0.02±0.0	0.01±0.0	0.02 ±0.0	0.02±0.0
Initial surface conditions: fine ground						
6	p-v (nm)	202±39	185±23	151±26	80±15	29±2
	rms (nm)	27±5	26±4	22±6	9±3	3±0.3
	Depth (μm)	1.9±0.03	2.2±0.05	1.6±0.03	1.7 ±0.02	1±0.06
	Vol. (mm <sup>3</sup> )	0.02±0.0	0.02±0.0	0.01±0.0	0.02 ±0.0	0.01±0.0

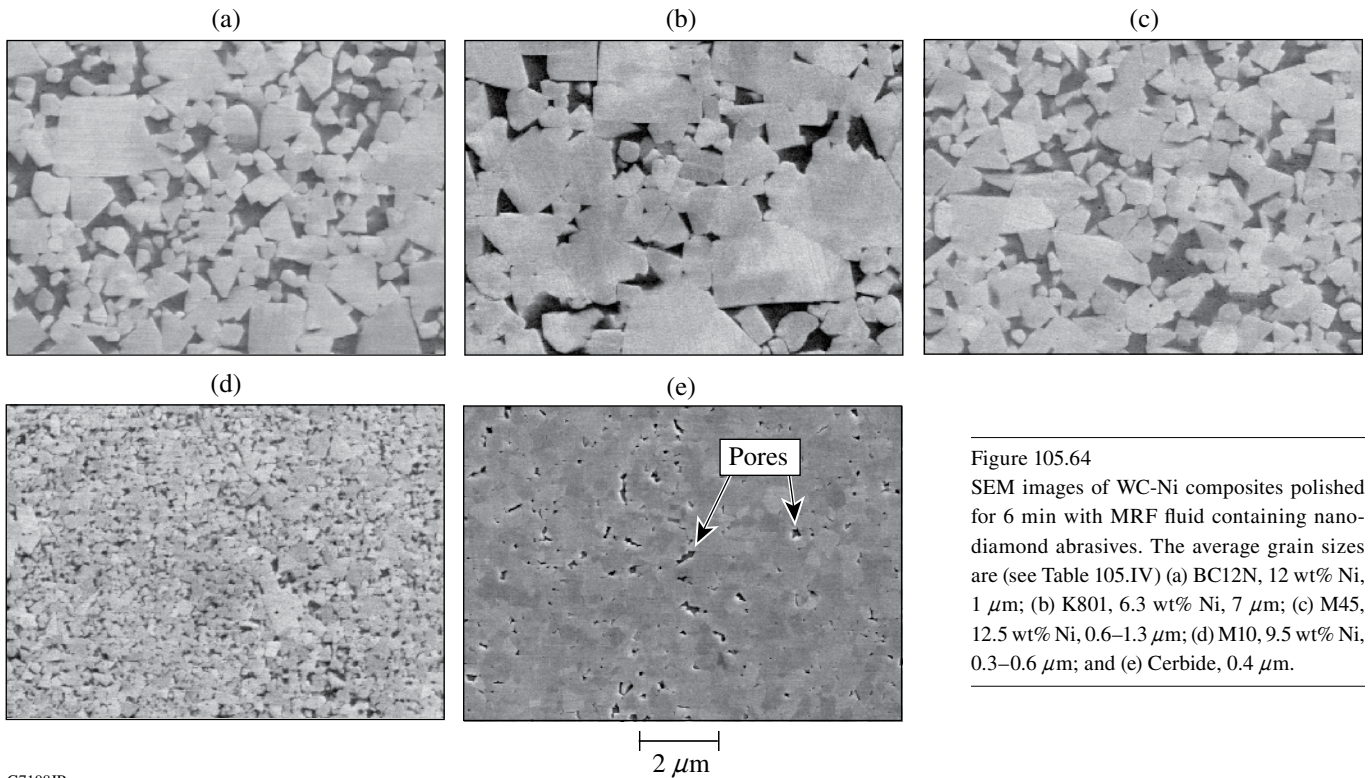


Figure 105.64  
SEM images of WC-Ni composites polished for 6 min with MRF fluid containing nano-diamond abrasives. The average grain sizes are (see Table 105.IV) (a) BC12N, 12 wt% Ni, 1  $\mu\text{m}$ ; (b) K801, 6.3 wt% Ni, 7  $\mu\text{m}$ ; (c) M45, 12.5 wt% Ni, 0.6–1.3  $\mu\text{m}$ ; (d) M10, 9.5 wt% Ni, 0.3–0.6  $\mu\text{m}$ ; and (e) Cerbide, 0.4  $\mu\text{m}$ .

G7108JR

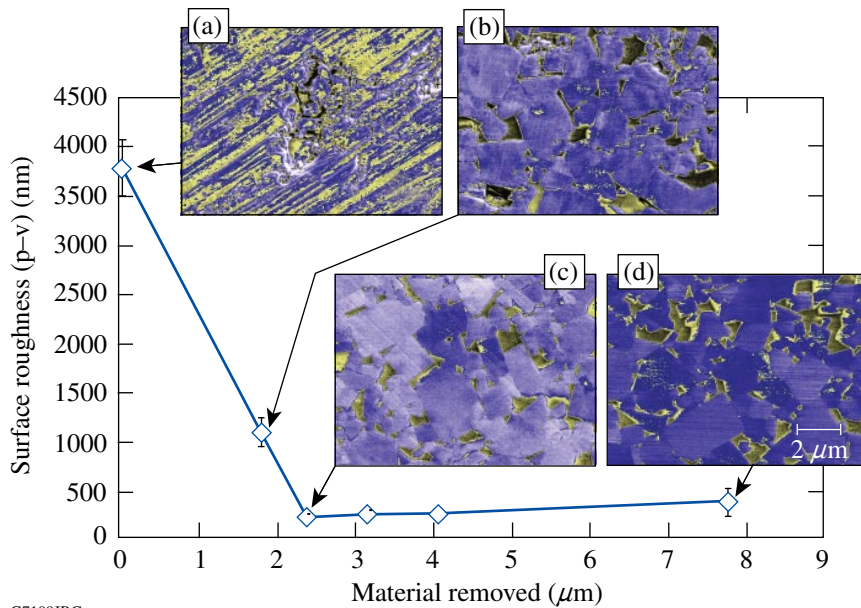
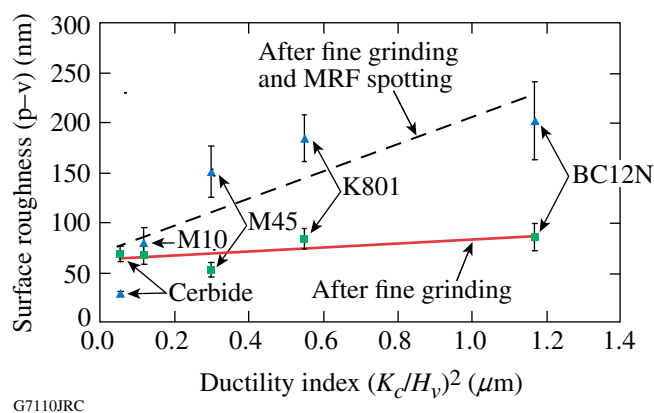


Figure 105.65  
Surface roughness in the MRF spots, p-v (nm), versus MRF spot material removal in microns for rough-ground K801. Each data point represents a spot time of as rough ground, 3, 6, 12, 18, and 40 min. The SEM images correspond to the (a) initial ground surface and (b) 1.8-, (c) 2.4-, and (d) 8- $\mu\text{m}$  material removed (within the spot ddp region). The error bars represent the standard deviation of five areal measurements.

G7109JRC

## Discussion

The results from the grinding experiments indicate no correlation between grinding-induced surface roughness and the materials' microstructure, i.e., Ni wt% or grain size, for all grinding conditions, as also observed by Yin *et al.*<sup>5</sup> In addition, surface roughness did not correlate well to the materials' hardness. As observed in the case of optical glasses under deterministic microgrinding conditions,<sup>18</sup> surface roughness correlates with the ductility index  $(K_c/H_v)^2$  (units of length) for both grinding and MRF processes conditions. Figure 105.66 shows that surface roughness values increased with increasing ductility index value. The true surface roughness is not well characterized as a result of heavily deformed material, fragmented WC, and tool residue over the ground surface.



G7110JRC

Figure 105.66

Surface-roughness measurements versus the materials' ductility index  $(K_c/H_v)^2$ . Data are for surfaces that were fine ground (correlation with ductility index has  $R^2 = 0.47$ ) or fine ground and subsequently MRF spotted (correlation with ductility index has  $R^2 = 0.70$ ).

Etching of the ground surface exposed some of the subsurface damage below the ground surface. SEM high-magnification images in the etching pits exposed cracks in WC grains of rough-ground surfaces, whereas for the medium- and fine-ground surfaces, removal was found to be within the ductile/plastic regime (see Fig. 105.61).

MRF spots are useful for analyzing both the material microstructure as well as for measuring the depth of the deformed surface layer from grinding. By removing an optimal amount of material (proportional to the initial p-v roughness in the rough-ground surfaces), the surface roughness is significantly reduced. However, additional material removal (beyond the optimal amount) resulted in a slight increase in surface roughness for materials with a high ductility index value. These results suggest that to completely remove the deformed surface

layer after rough grinding ( $\sim 40\text{-}\mu\text{m}$  grit size), an amount of material equivalent in depth to the initial p-v surface roughness that needs to be polished/removed. For the materials tested, removing the initial p-v surface roughness values was sufficient to completely eliminate the damaged/deformed surface layer with the exception of WC M10, which showed a monotonic decrease of roughness with the amount of material removed. The increase in surface roughness for the Cerbide can be explained in Fig. 105.64(e), which clearly shows some degree of porosity at the carbide boundaries.

The effect of the initial surface roughness from grinding with rough, medium, or fine tools on the MRF performance is shown in Tables 105.VI and 105.VII. Initial ground surface conditions, either coarse or fine, had a small effect on the resulting surface roughness inside the MRF spot for materials with a high ductility index. The p-v and rms surface roughness improved with a decreasing ductility index for initial fine-grind conditions. However, we found that MRF spot surface roughness was higher than the initial fine-ground surface, e.g., from  $\sim 86$  nm (BC12N) after fine grinding to  $\sim 202$  nm (BC12N) following MRF removal in the range of 1 to  $2.2\ \mu\text{m}$ .

Further investigation of surface response inside a MRF spot for materials with a high ductility index was done to investigate the eventual slight increase of roughness with the amount of material removed. Figure 105.65 suggests that additional spot time promotes preferential polishing of the nickel binder, which resulted in increasing surface-roughness values. The effect of preferential polishing on surface roughness is also known as grain decoration.<sup>31</sup> A selective AFM scan demonstrates preferential polishing/grain decoration on the resulting surface roughness inside the MRF spot. Figure 105.67(a) shows AFM scans from the ddp in K801 ( $7\text{-}\mu\text{m}$  average grain size) after an optimal  $2.4\text{-}\mu\text{m}$  amounts of material have been recovered (pit depth in the range of 9 to 12 nm), while Fig. 105.67(b) shows the development of preferential grain decoration when an excessive amount ( $8\ \mu\text{m}$ ) has been removed (pit depth in the range of 27 to 61 nm). These features show that MRF spot-derived material removal can be optimized to remove the damaged layer at the surface without acceleration grain decoration. Excessive amounts of MRF removal may lead to grain decoration in a material with a higher ductility index. On the other hand, materials with a lower ductility index like M10 may show a monotonic reduction to surface roughness with the amount of material removed by MRF. This represents true polishing of this material, a desired outcome for the manufacture of mold masters or other optics from WC.

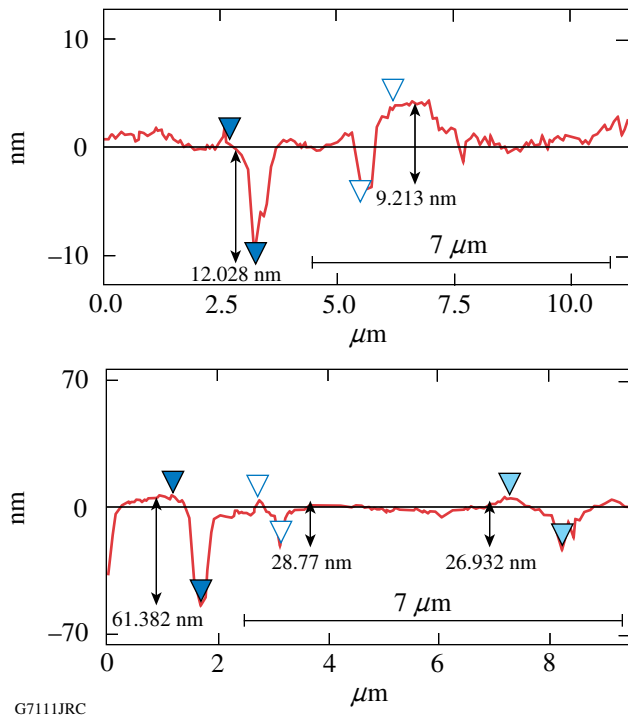


Figure 105.67  
 AFM surface profiles from the ddp region of a MRF spot taken on K801 (average grain size 7 μm). (a) 2.4 μm and (b) 8 μm were removed. The initial surfaces were rough ground and had a p–v surface roughness of 3.8 μm. The double arrows represent the vertical distance between markers and the scale bar represents the average grain size.

### Conclusions

We have studied the response of five nonmagnetic WC composites to deterministic microgrinding. Grinding experiments showed that grinding-induced surface roughness decreased with decreasing diamond abrasive size. Microgrinding with a rough tool (40-μm grit size) involved fracture, leading to a p–v surface roughness in the range of 3.2 to 5.8 μm (150- to 700-nm rms). Microgrinding with medium and fine tools (10- to 20-μm and 2- to 4-μm grit size, respectively) was controlled by plastic flow. The medium tool led to p–v surface roughness values in the range of 0.5 to 3.8 μm (27- to 200-nm rms), whereas the fine tool resulted in surface p–v values in the range of 53 to 86 nm (7- to 13-nm rms). The true grinding-induced surface roughness was concealed by the deformed layer on the ground surface.

We have demonstrated that a MRF spot can be placed on ground surfaces of tungsten carbide and that the spot can be used to evaluate the depth of the surface deformed layer. For the rough and medium tools, the deformed layer is in the range 1.5- to 2.7-μm. The surface roughness of MRF spot at the deepest point of penetration can be used as a guide for estab-

lishing the optimal amount of material to be removed by MRF. Optimal MRF removal indeed removes the deformed surface layer caused by grinding. Excessive MRF removal may lead to preferential polishing and removal of the binder phase, also known as grain decoration. By utilizing both surface-roughness measurements and SEM imaging at the spot ddp, we were able to estimate the depth of the deformed layer. Thus, we showed that the depth of the deformed layer can be estimated in two ways. An optical profilometer-based measurement of the p–v surface microroughness of the ground surface provides an upper bound to the deformed layer thickness. This is a desirable estimate given the noncontact nature of this metrology technique. On the other hand, the MRF spot can also be used to reveal the depth of the deformed layer while reducing the surface roughness.

### ACKNOWLEDGMENT

The authors thank A. Shorey of QED Technologies in Rochester, NY, for the use of the AFM and K. Muir of the Laboratory for Laser Energetics Summer High School Research Program for surface-roughness measurements. The authors acknowledge the Laboratory for Laser Energetics at the University of Rochester for its continuing support. One of the authors (S. Shafir) is a LLE Horton Fellow. This work was supported by the U.S. Department of Energy Office Confinement Fusion under Cooperative Agreement No. DE-FC52-92SF19460, the University of Rochester, and the New York State Energy Research and Development Authority. The support of DOE does not constitute an endorsement by DOE of the views expressed here.

### REFERENCES

1. G. S. Upadhyaya, *Cemented Tungsten Carbides: Production, Properties, and Testing*, Materials Science and Process Technology Series (Noyes Publications, Westwood, NJ, 1998).
2. G. Wirmark and G. Dunlop, in *Science of Hard Materials*, edited by R. K. Viswanadham, D. J. Rowcliffe, and J. Gurland (Plenum Press, New York, 1983), pp. 311–338.
3. J. Larsen-Basse, *J. Mater.* **35**, 35 (1983).
4. S. Imasato *et al.*, *Int. J. Refract. Met. Hard Mater.* **13**, 305 (1995).
5. L. Yin *et al.*, *Int. J. Mach. Tools Manuf.* **44**, 533 (2004).
6. W. K. Chen *et al.*, *Precis. Eng.* **29**, 315 (2005).
7. L. Yin *et al.*, *Proc. Inst. Mech. Eng. B, J. Eng. Manuf.* **218**, 419 (2004).
8. J. Larsen-Basse and N. Devnani, in *Science of Hard Materials*, edited by E. A. Almond, C. A. Brookes, and R. Warren, Institute of Physics Conference Series, No. 75 (Hilger, Bristol, England, 1986), pp. 883–895.
9. J. Larsen-Basse, in *Science of Hard Materials*, edited by R. K. Viswanadham, D. J. Rowcliffe, and J. Gurland (Plenum Press, New York, 1983), pp. 797–813.

10. W. Precht, R. K. Viswanadham, and J. D. Venables, in *Science of Hard Materials*, edited by R. K. Viswanadham, D. J. Rowcliffe, and J. Gurland (Plenum Press, New York, 1983), pp. 815–828.
11. J. B. J. W. Hegeman, J. Th. M. De Hosson, and G. de With, *Wear* **248**, 187 (2001).
12. J. A. Randi, J. C. Lambropoulos, and S. D. Jacobs, *Appl. Opt.* **44**, 2241 (2005).
13. Basic Carbide, Lowber, PA 15660.
14. Kennametal, Inc., Charlotte, NC 28273.
15. Fuji Die Co., Ltd., Ota-ku, Tokyo, Japan.
16. Materials tested were commercially available in January 2005, Cerbide, Inc., Orchard Park, NY 14127.
17. J. Larsen-Basse, in *Tribology—Friction, Lubrication and Wear, Fifty Years On: Proceedings of the Institution of Mechanical Engineers, International Conference* (Mechanical Engineering Publications Ltd., Bury St. Edmunds, Suffolk, 1987), pp. 277–282.
18. J. C. Lambropoulos, T. Fang, P. D. Funkenbusch, S. D. Jacobs, M. J. Cumbo, and D. Golini, *Appl. Opt.* **35**, 4448 (1996).
19. A. G. Evans, in *Fracture Mechanics Applied to Brittle Materials*, edited by S. W. Freiman (American Society for Testing and Materials, Philadelphia, 1979), Vol. ASTM STP 678, Part 2, pp. 112–135.
20. M. T. Laugier, *J. Mater. Sci. Lett.* **6**, 768 (1987).
21. OptiPro Systems, Ontario, NY 14519.
22. Opticut GPM 5% in water, pH 9–10, Lighthouse Lubricant Solutions, LLC, Overland Park, KS 66282.
23. S. D. Jacobs, H. M. Pollicove, W. I. Kordonski, and D. Golini, in *International Conference on Precision Engineering, ICPE '97* (ICPE, Taipei, Taiwan, 1997), pp. 685–690.
24. A. B. Shorey, S. D. Jacobs, W. I. Kordonski, and R. F. Gans, *Appl. Opt.* **40**, 20 (2001).
25. S. R. Arrasmith, I. A. Kozhinova, L. L. Gregg, A. B. Shorey, H. J. Romanofsky, S. D. Jacobs, D. Golini, W. I. Kordonski, S. J. Hogan, and P. Dumas, in *Optical Manufacturing and Testing III*, edited by H. P. Stahl (SPIE, Bellingham, WA, 1999), Vol. 3782, pp. 92–100.
26. S. D. Jacobs, *Finer Points* **7**, 47 (1995).
27. Zygo NewView™ 5000 White Light Interferometer, Zygo Corporation, Middlefield, CT 06455.
28. Taylor Hobson TalySurf 2 PGI profilometer, 120-mm traverse unit, 10-mm gauge range, 12-nm vertical resolution, and 0.1- $\mu$ m accuracy. Stylus specifications: 60° tip angle and 2- $\mu$ m tip radius, Taylor Hobson, Inc., Rolling Meadows, IL 60008-4231.
29. Digital Instruments/Veeco Metrology Dimension 3100S-1 Atomic Force Microscope, Veeco Instruments, Inc., Woodbury, NY 11797-2902.
30. S. Tong, “Chatter in Contour Deterministic Microgrinding,” Ph.D. thesis, University of Rochester, 2004.
31. L. L. Gregg, A. E. Marino, J. C. Hayes, and S. D. Jacobs, in *Optical Manufacturing and Testing V*, edited by H. P. Stahl (SPIE, Bellingham, WA, 2004), Vol. 5180, pp. 47–54.
32. M. T. Laugier, *J. Mater. Sci. Lett.* **6**, 779 (1987).
33. M. T. Laugier, *J. Mater. Sci. Lett.* **6**, 897 (1987).